

Ice Accretion Roughness Measurements and Modeling

Stephen T. McClain*, Mario Vargas**, Jen-Ching Tsao[§], Andy P. Broeren**, and Sam Lee[†]

*Baylor University

One Bear Place #97356, Waco, TX 76798-7356

**NASA Glenn Research Center

21000 Brookpark Rd., MS 11-2, Cleveland, OH 44135

[§]Ohio Aerospace Institute

21000 Brookpark Rd., MS 11-2, Cleveland, OH 44135

[†]Vantage Partners, LLC

21000 Brookpark Rd., MS 11-2, Cleveland, OH 44135

Abstract

Roughness on aircraft ice accretions is very important to the overall ice accretion process and to the resulting degradation in aircraft aerodynamic performance. Roughness enhances the local convection leading to more rapid ice accumulation rates, and roughness generates local flow perturbations that lead to higher skin friction. This paper presents 1) a review of the developments in ice shape three-dimensional laser scanning developed at NASA Glenn, 2) a review of the approach of McClain and Kreeger employed to characterize ice roughness evolution on an airfoil surface, and 3) a review of the experimental efforts that have been performed over the last five years to characterize, scale, and model ice roughness evolution physics.

1. Introduction

Roughness that forms during the initial stages of an icing encounter is thought to be very important to the overall ice accretion process and to the resulting degradation in aircraft performance. This expectation is based on the facts that 1) the roughness enhances the local convection leading to more rapid ice formation rates and 2) the roughness generates local flow perturbations that lead to higher skin friction and potentially force the boundary-layer flow to prematurely transition to turbulence.

Because of its importance to the overall aircraft ice accretion process, measuring and modeling of the physical characteristics of roughness and its evolution during the ice accretion process has been the subject of many investigations. However, because of the material properties of all ice accretions and because of the optical nature of glaze ice, measuring ice roughness has presented many challenges. Traditional diamond-tipped stylus profilometers will chip and scratch the brittle ice surface, and optical and laser-based profilometers will exhibit spurious measurements because of reflections and refraction of light caused by the nearly-clear glaze ice.

To circumvent the issues with traditional profilometry techniques, past investigations have employed 1) digitized pencil tracing analysis [1], 2) profilometry on cast replicas of ice shapes [2-6], and 3) multiple-angle, photogrammetric approaches [7-9]. While the past alternative approaches have illuminated many features of icing roughness, each approach has issues. The pencil tracing approaches are tedious and limited in their ability to properly sample the ice features; casting replicas may experience expansion or shrinkage of the mold or model relative to the original ice shape and often exhibit errors in the surface replication caused by bubbles in the resin or by liquidity issues in proper filling of the molds and crevasses created by the roughness elements [10]; and photogrammetric approaches result primarily in morphological descriptions of roughness that are often difficult to convert to parameters typically used for aerodynamic and heat transfer predictions such as equivalent sand-grain roughness.

To predict ice accretion rates on airfoil surfaces, ice accretion modeling codes such as LEWICE [11], must employ both a roughness geometry model and a convective enhancement model. Given the limitations in the past ice roughness measurement processes, roughness geometry evolution modeling in many ice accretion codes is an opportunity for improvement or a mechanism for fine-tuning predictions. LEWICE, for example, employs a conservative approach that imposes the equivalent sand-grain roughness height during an ice accretion simulation for all time steps based solely on the stagnation point freezing fraction. While this approach neglects many fine details of ice roughness evolution, the model is sufficiently generalized and calibrated to capture ice accretion evolution over a wide range of conditions [11].

Recently, the process of laser-based three-dimensional scanning of ice shapes employed in the Icing Research Tunnel (IRT) at NASA Glenn Research Center has matured enabling new insights into icing physics. Lee et al. [12], Lee et al. [13], Broeren et al. [14], and Kreeger and Tsao [15] represent the chronology of the acquisition, initial uses, refinements, and common use of laser scanning of airfoils and wings with accreted ice formations. As the laser scanning system was maturing, the self-organizing map (SOM) based approach of McClain and Kreeger [16] was developed to extract the highly curved ice accretion shape or “form” from the point cloud and characterize the roughness variations along the surface of an airfoil. The approach of McClain and Kreeger [16] has subsequently been used to characterize roughness on unswept and swept symmetric airfoils with no angle of attack in Appendix C and supercooled large droplet (SLD) conditions [17-19]. The investigation of McClain et al. [20] focused on scaling of roughness properties between NACA 0012 airfoils with different chord.

The results of the laser-based 3D-scanning ice roughness studies have provided new insights into the physics of ice roughness evolution. The purpose of this paper is to provide a review of the ice accretion measurement method, the roughness characterization approach, and the roughness evolution model developed during the recent roughness characterization studies. Limitations of the measurements and modeling approach will be discussed, and experiments with the potential to improve the resulting correlations will be described.

2. Laser-Based 3D Scanning Method in the IRT

The 3D laser scanner currently in use in the IRT is the Romer 7530SI articulating arm with an integrated laser scanner. The system consists of a laser scan head that is mounted on the end of a 7-axis arm which the operator positions manually. Absolute encoders, which are built into the arm, track the location of the scanner head relative to the base of the arm. The 3D laser scan data are then referenced to the location of the base of the arm. The system has a measurement reach of 9 ft., allowing it to digitize a large portion of the wind tunnel model from a single location. The scanner projects a scan line 2.3-in wide, with a maximum resolution of 0.002 in. The Romer scanner is operated directly from *Geomagic Wrap* software through a plug-in. The scanner is also fitted with a hard-probe for tactile-based, single-point measurements that is used to capture model reference points. Five reference points (consisting of counter-sunk holes) are typically drilled into the surface of the model. These are used to obtain an airfoil model-based coordinate system

After the ice is accreted on the model, it is coated with highly-reflective, diffuse, white paint using an automotive-style spray gun, as depicted in Figure 1. After the ice is painted, the scanner and the laptop computer to control the scanner are brought into the test section. The ice is scanned until a sufficient level of detail has been captured over the airfoil model in the center 6-in. section of the test section. The final step in the scanning procedure is to acquire the hard probe points of the five reference holes for alignment to the airfoil model-based coordinate system.



Figure 1. Painting an Ice Accretion in the Icing Research Tunnel at NASA Glenn

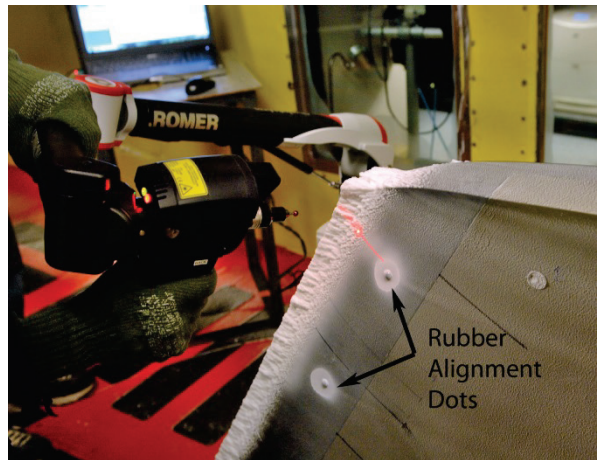


Figure 2. Scanning an Ice Accretion in the Icing Research Tunnel at NASA Glenn

The ice accretion scan data are processed into water-tight surfaces using *Geomagic Wrap*. The scanned ice accretion is comprised of multiple ordered point cloud objects (each from individual scan passes). Typically 10 to 30 scan passes are required to capture a single ice shape. The first step in processing the scan data is to align the scan objects using the Global Registration feature within *Geomagic Wrap*. Global Registration reorients the scan objects so that the common or shared regions coincide. The next step is to combine the numerous point-scan objects into a single point cloud object. This process also removes all of the overlap regions. The point cloud data are then

converted into a triangular surface mesh (constructed of connected triangles) using the Wrap feature. Any defects in the mesh (including holes) are repaired using the Mesh Doctor and hole-filling tools. The coordinate system of the mesh is then converted to one based on the airfoil model by aligning the hard-probe reference points to the known coordinates on the model. The final step is to convert the Geomagic mesh file into a solid model file, such as a stereolithography file (*.STL), for use in other CAD programs.

An example of a three-dimensional laser of an ice shape created in the IRT with significant roughness is presented in Figure 3. The ice shape of Figure 3 was acquired on a 91.44-cm (36-in.) chord NACA 0012 swept at an angle of 30° with zero angle of attack. The cloud exposure time, Δt_s , was 340 seconds, and the cloud conditions used were $T_{total} = -2.3$ °C, $V = 67$ m/s (130 knots), $LWC = 0.60$ gm/m³, and $n = 0.22$. The ice shape is identified with the run number 031414.01. The unswept-wing accumulation parameter for the 031414.01 case, defined as:

$$A_c = \frac{LWC \cdot V \cdot \Delta t_s}{2 \cdot r_0 \cdot \rho_{ice}} \quad (1)$$

was 0.516. This value of accumulation parameter is near the limit of what may be considered early-stage ice before the ice shape begins to exhibit significant two-dimensional or three-dimensional features such as horns, scallops or lobster-tails. While the 031414.01 case is close to the “early-stage” limit and while most of the ice roughness investigations have been performed at accumulation parameters less than 0.5 [17-20], the ice shape is still considered a predominately “roughness” ice shape, and the larger roughness features enable clear visualization of the roughness results that will be presented in the following sections.

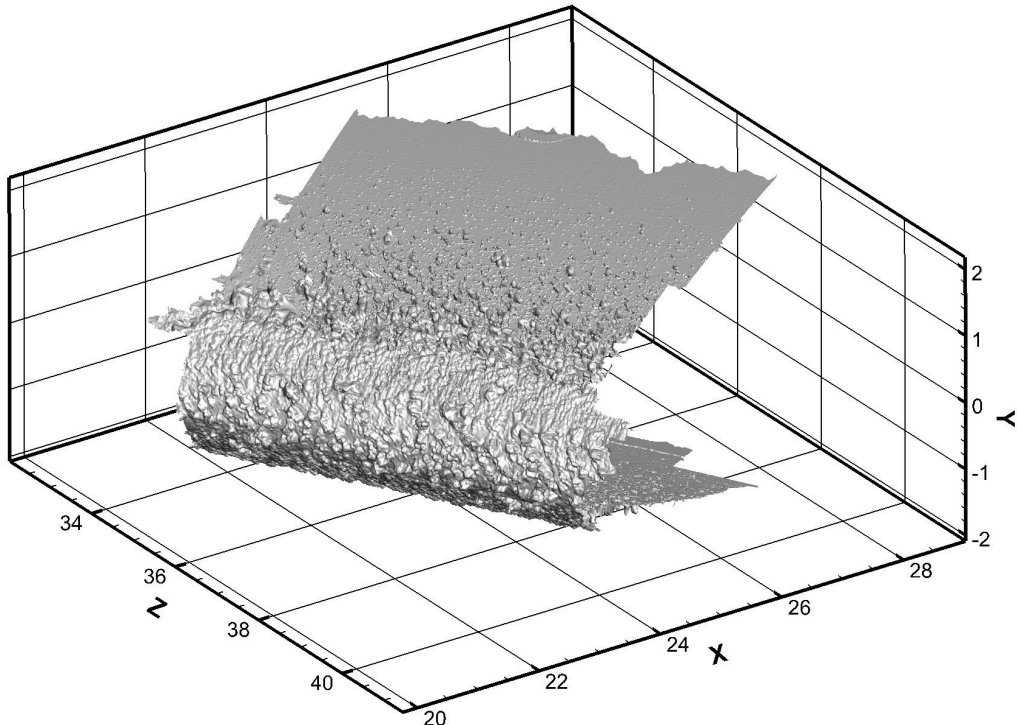


Figure 3. Visualization of the Water-Tight 3D Laser-Scan Representation of the 031414.01 Ice Shape in Wind-Tunnel Coordinates (All dimensions shown are in inches.)

3. SOM-Based Roughness Analysis

The self-organizing map (SOM), or sometimes referred to as a Kohonen Map, is a clustering method for the detection of non-linear manifolds, which may be curves or surfaces, in multi-dimensional space [21]. SOMs depend on the use of codebook vectors, \mathbf{b} , which may also be called codebook points or neurons, to represent clumps of data. Following convergence of the SOM method, each codebook vector will be located at the spatial centroid of the clump of data that it represents. A set of codebook vectors representing clumps of data points is depicted on the top half of Figure 4. In its simplest essence, self-organizing maps are employed to capture trends of large data sets by representing those large data sets by a relatively small set of codebook vectors.

To capture the trends of a large data set, an SOM algorithm begins by distributing a number of codebook vectors randomly through the space contained by the data set. The codebook vectors are then sequentially moved in

the direction of the clump of data points that are closest to the codebook vector. Like most neural network approaches, the SOM requires a learning or training process. Over iterative moves, the codebook vectors spread out and settle into their local clumps. When a series of codebook vectors are connected in a sequence, as shown on the right side of Figure 4, the representative manifold, or curve as is the case in Figure 4, guiding the data through the data space is represented by the imposed path connecting the discrete codebook vectors. For more detailed information on self-organizing maps and their application for iced airfoil description and roughness evaluation, please consult Refs. [16] and [22].

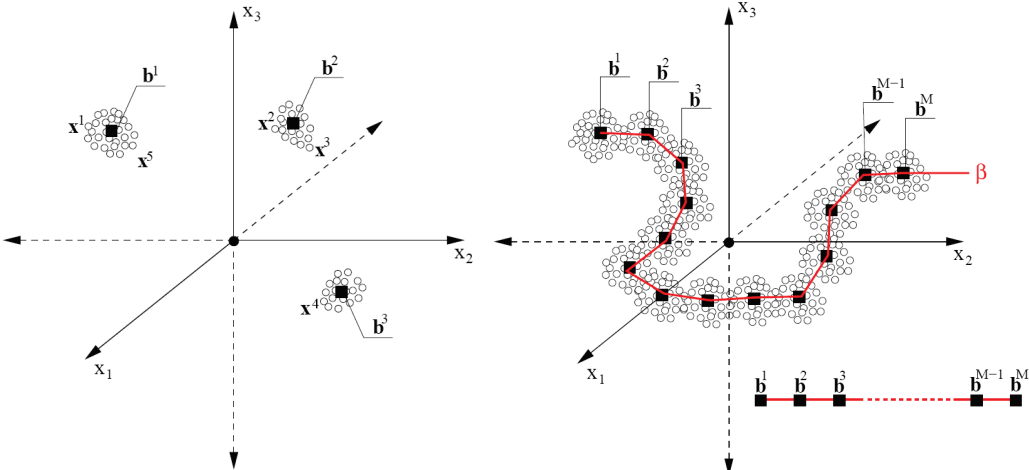


Figure 4. Self-Organizing Map Representation of Point Cloud [16]

When applied to an iced airfoil without sweep or significant spanwise shape changes, the SOM is expected to identify a curve in the Chord-Chord Normal plane (or X' - Y' plane in the airfoil coordinates where the spanwise axis is the Z' -direction), which represents the mean shape of the rough airfoil. Figure 5 demonstrates the resulting codebook vector positions in the projected airfoil coordinates for the 031414.01 ice shape.

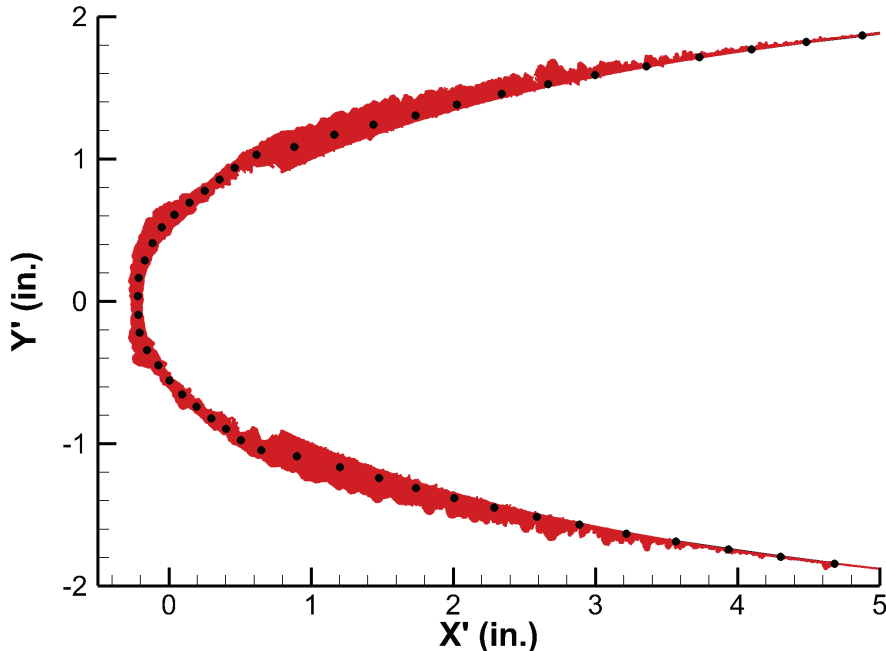


Figure 5. Projected Point Cloud (Red Points) and Codebook Vector Representation (Black Points) for the 031414.01 Ice Shape

The nature of the SOM method and the positioning of the codebook vectors along a “daisy-chain” enable a statistical evaluation of iced airfoil surface roughness. Since the “clumps” of points are distributed about the

codebook vectors, the deviations of the point measurements in the clumps can be used to evaluate the coverage statistics and uncertainty of the codebook vector representation. Figure 6 demonstrates how each surface measurement is used to determine a deviation from the spline surface through the control points or codebook vectors.

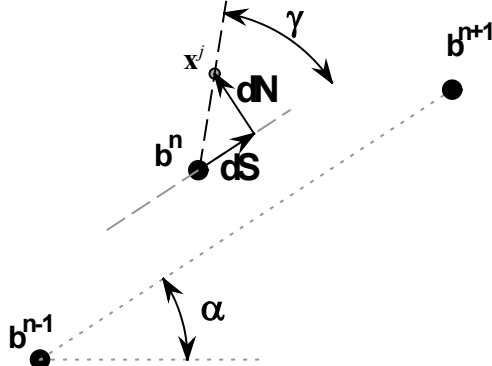


Figure 6. Metrics of Local Point about a Codebook Vector [16]

Figure 6 shows a single surface measurement, x^j , and its closest codebook vector b^n . The two neighboring codebook vectors along the daisy-chain of codebook vectors representing the manifold are also shown. In the approach used for this study, the manifold is assumed to be a first-order manifold in two-dimensional space with the characteristic that at each codebook vector the local slope of the manifold is equal to the central finite-difference evaluated using the two closest surrounding codebook vectors. The approach used assumes that all deviations from the manifold are normal to the manifold. That is, the deviation of a surface measurement normal to the line through the codebook vector with the local slope set by the neighboring codebook vectors is considered the “height” of the surface point above or below the local manifold.

To calculate the local height of any point, x^j , relative to the manifold, the two neighboring codebook vectors are first used to calculate the direction of the manifold through b^n using

$$\alpha_{b^n} = \arctan \left[\frac{y_{b^{n+1}} - y_{b^{n-1}}}{x_{b^{n+1}} - x_{b^{n-1}}} \right] \quad (2)$$

The direction of the x^j point from its closest codebook vector relative to the line through the codebook vector with the direction α is then found using

$$\gamma_{x^j} = \arctan \left[\frac{y_{x^j} - y_{b^n}}{x_{x^j} - x_{b^n}} \right] - \alpha_{b^n} \quad (3)$$

The normal height of the x^j point from the line through its closest codebook vector is then determined using

$$N_{x^j} = \left[(x_{x^j} - x_{b^n})^2 + (y_{x^j} - y_{b^n})^2 \right]^{\frac{1}{2}} \sin(\gamma_{x^j}) \quad (4)$$

The surface heights from the mean elevation from Eq. (4) may be used to create topography maps of the ice roughness. Figure 7(a) presents the topography of the 031414.01 ice shape color-mapped by the normal height from the mean elevation as defined by the codebook vectors. If the original airfoil design coordinates are used in Figure 6 and in Eqns. (2)-(4), then the ice thickness relative to the clean airfoil surface may also be determined. Figure 7(b) presents the ice thickness measurements for the 031414.01 ice shape. Further details regarding the ice thickness measurements method and the distinction between ice roughness and thickness may be found in McClain [23].

The normal height of all the points related to an individual codebook vector may then be used to calculate statistics such as those commonly used to calculate traditional roughness parameters. For example, the root-mean-square roughness height for a rough surface is traditionally described as

$$R_q = \left[\frac{1}{J} \sum_{j=1}^J (y_j - \bar{y})^2 \right]^{\frac{1}{2}} \quad (5)$$

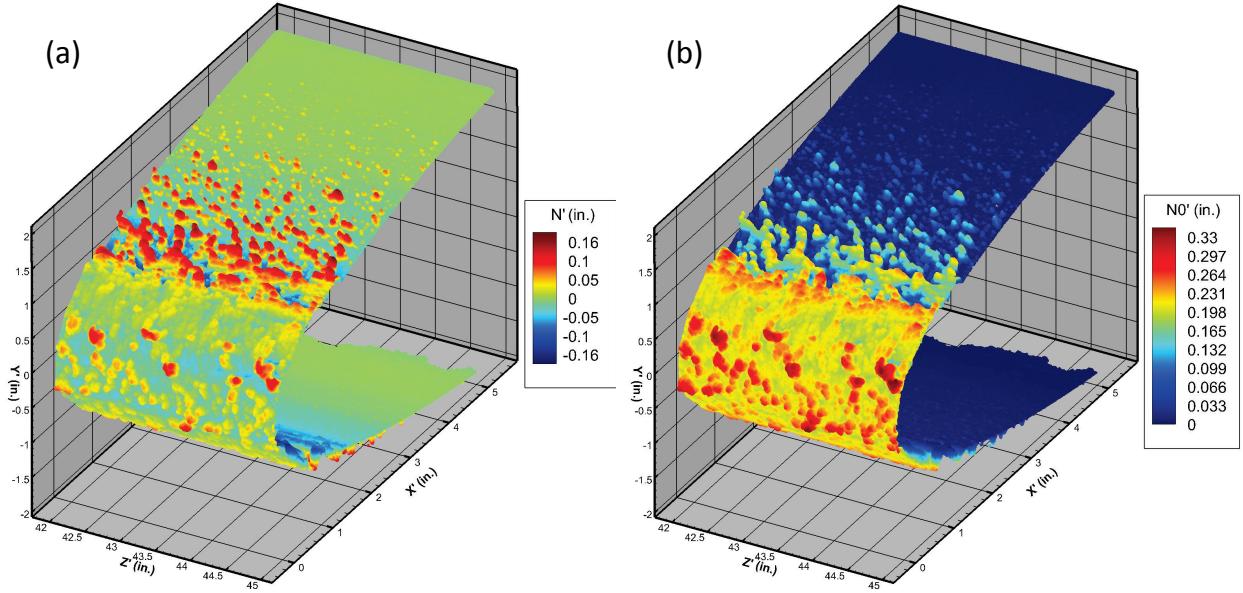


Figure 7. Topography Visualization of the 031414.01 Ice Surface: (a) Roughness and (b) Thickness

Based on the SOM-manifold description used here, the root-mean-square roughness height is calculated at each codebook vector as

$$R_q = \left[\frac{1}{J} \sum_{j=1}^J N_{x^j}^2 \right]^{\frac{1}{2}} \quad (6)$$

In some roughness studies, the 99.9% roughness maximum height (RMH) based on a Gaussian distribution is calculated using 3.09 times the root-mean roughness height.

$$RMH_{b^n} = 3.09 R_q = 3.09 \left[\frac{1}{J} \sum_{j=1}^J N_{x^j}^2 \right]^{\frac{1}{2}} \quad (7)$$

Where J is the number of surface points for which b^n is the winning (closest) codebook vector. The RMH is the *local* 99.9%-maximum roughness height and is evaluated at each codebook vector based on the local or neighborhood statistics. The RMH will vary along the surface arc length.

While the RMH is not a universal roughness descriptor, the RMH value has been employed extensively in the prior ice roughness investigations [17-20]. Since the RMH represents a Gaussian prediction of the 99.9% maximum distance from the mean elevation to the tallest peaks in a data set, the RMH is a reasonable tool to compare the statistical results to the morphological descriptors such as roughness element diameter and height used in the historical roughness studies. Further, the RMH values may be thought of as the 99.8% (two-tailed) Gaussian inclusion limits of the neighborhood points normal to the mean ice shape manifold. Figure 8 presents a demonstration of the 99.8% inclusion limits for the 031414.01 ice shape. In Figure 8, each neighborhood of the codebook vectors is assigned a different color. The vectors emanating from the codebook vector locations extend normal to the local manifold representing the mean ice shape and have a length equal to the RMH value evaluated at each codebook vector. If the neighborhoods are distributed around the codebook vectors and manifold in a Gaussian distribution, only 0.2% (1 of 500) will be outside the RMH inclusion limits.

To evaluate the distance along the manifold representing the mean ice shape, a discrete arc-length approach is taken. That is, at one end of the daisy chain, the length of the arc is set to zero or a known value from the stagnation point on the airfoil. The position of the next codebook vector is then evaluated as the straight-line distance between the two codebook vectors as demonstrated in Eq. (8).

$$S_{b^n} = S_{b^{n-1}} + \left[(x_{b^n} - x_{b^{n-1}})^2 + (y_{b^n} - y_{b^{n-1}})^2 \right]^{\frac{1}{2}} \quad (8)$$

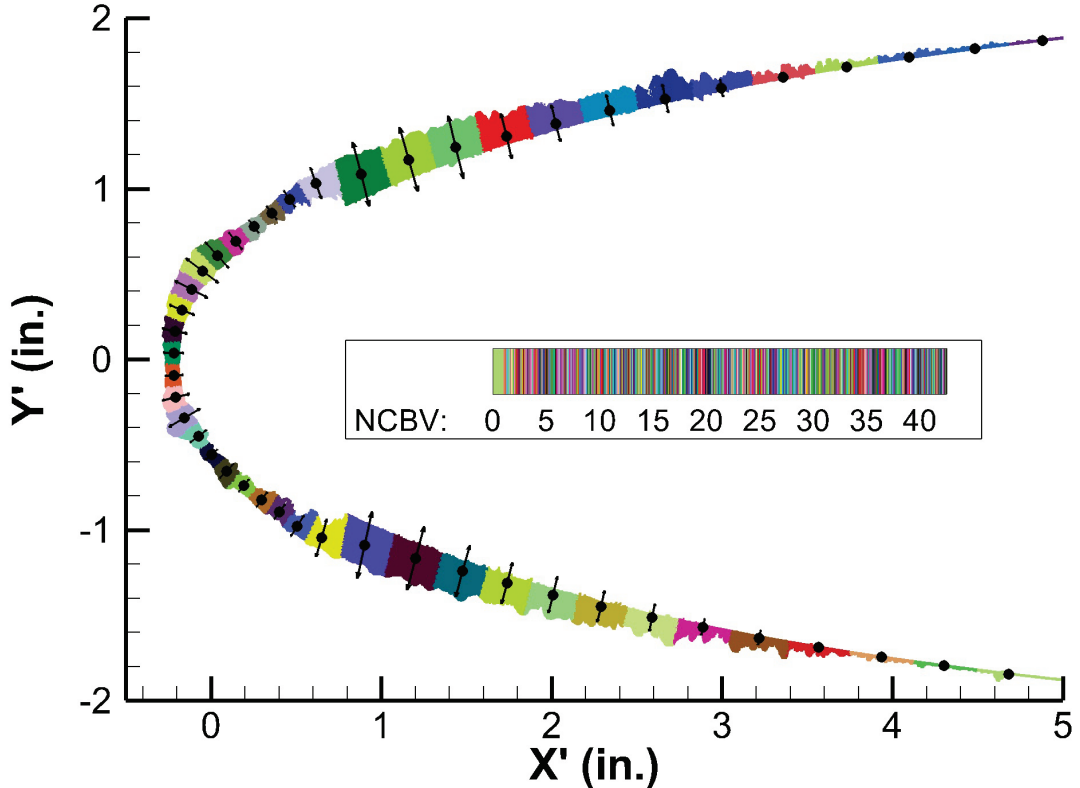


Figure 8. 031414.01 Point Cloud and 99.8% Gaussian Inclusion Limits

Once the surface distance coordinate of each codebook vector is determined, the surface distance coordinate of each point cloud measurement may be evaluated based on the location of the surface point's winning codebook vector. Revisiting Figure 6, once the angle of the x^j point with respect to the surface manifold through its winning codebook vector (γ) is known, the surface projection along the manifold is found using

$$S_{x^j} = S_{b^n} + dS_{x^j} = S_{b^n} + \left[(x_{x^j} - x_{b^n})^2 + (y_{x^j} - y_{b^n})^2 \right]^{\frac{1}{2}} \cos(\gamma_{x^j}) \quad (9)$$

The straight-line arc length approach of Eq. (8) is not the only option for evaluating the length of the manifold between the codebook vectors; however, the method employing Eqns. (8) and (9) captures the salient features of any unwrapping process. Those critical features being 1) the distance between the codebook vectors along the manifold are calculated and then 2) the projected distance of each surface point from its winning codebook vector is calculated relative to the directions tangent to and normal to the manifold passing through the winning codebook vector.

Based on the codebook vector surface distance calculations of Eq. (8), the ice roughness and thickness variations may be investigated in terms of the surface distance from the leading edge. Figure 9 presents the roughness statistics and mean thickness measurements evaluated at each codebook vector for the 031414.01 ice shape. Figure 9(a) demonstrates two thickness regions on swept-wing, early-stage glaze ice accretions: 1) a smoother region near the leading edge and 2) a region aft of the leading edge region where the roughness values increase abruptly and then decay with increasing surface distance from the leading edge. Comparing Figures 9(a) and 9(b), the thickness variations of Figure 9(b) indicate that the first roughness region occurs on top of the glaze-ice plateau, which is the region of continuous clear ice on the leading edge of the wing of nearly constant thickness in Figure 9(b), while the second roughness region begins just downstream of the edge of the glaze-ice plateau.

Finally, the surface distance of each surface in the laser-scan point cloud, calculated in Eq. (9) may be used to create unwrapped or “geodesic” visualizations of the ice roughness, as shown in Figure 10 for the 031414.01 case. The geodesic visualizations demonstrate roughness element connectivity and directionality. Figure 10 demonstrates that the roughness elements on the swept 91.44-cm NACA 0012 of the 031414.01 case are starting to align diagonally in a way that resembles the nature of scallops and lobster tails that might form in later ice accretion times.

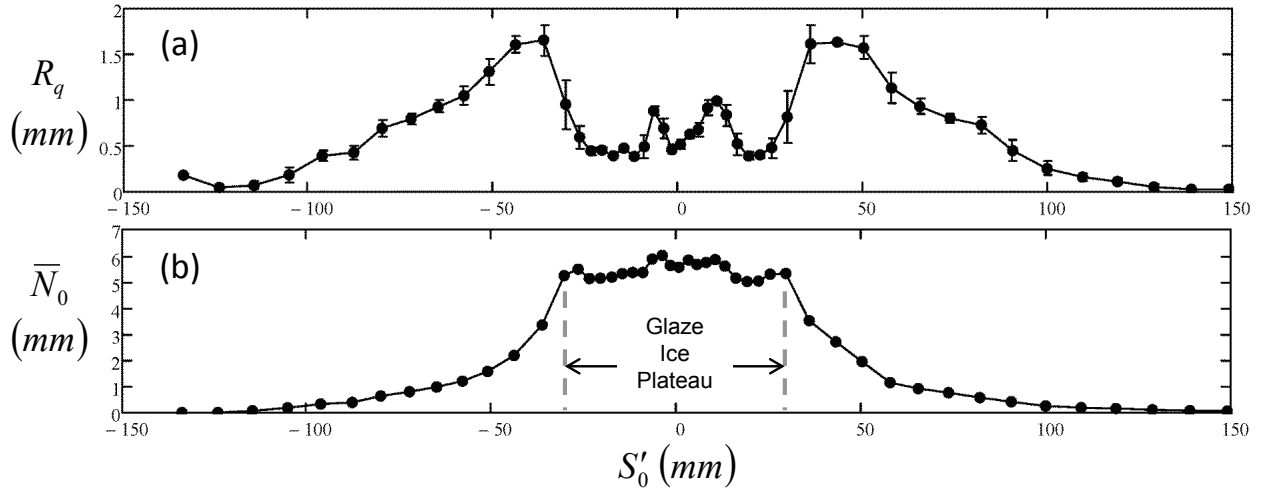


Figure 9. Reduced Roughness (a) and Thickness (b) Variations along the 031414.01 Ice Surface

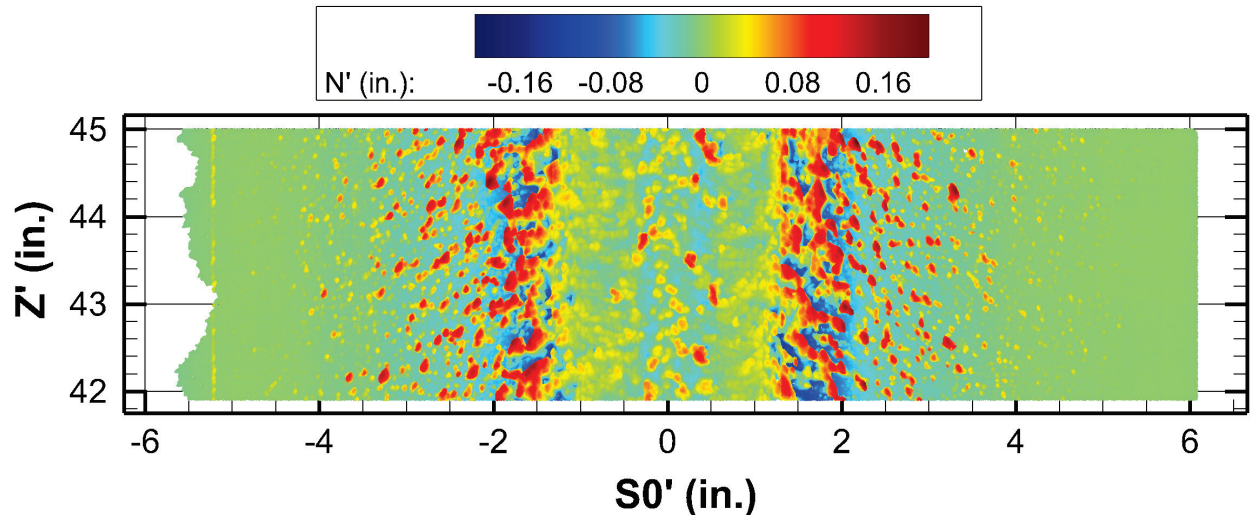


Figure 10. Unwrapped or Geodesic View of Roughness on 031414.01 Ice Shape

4. Roughness Spatial and Temporal Evolution Modeling

Following the development of the 3D laser scanning method in the IRT, the SOM-based roughness characterization development of McClain and Kreeger [16], An initial series of investigations [17-18] was performed replicating conditions used in prior roughness studies in the IRT [7-9]. Subsequently, a modeling effort was initiated by McClain et al. [19] for two unswept NACA 0012 airfoils with different sized chords. The implementation of the modeling approach was then continued by McClain et al. [20] for a NACA 0012 wing with 30°-sweep.

The objective of the modeling effort is to develop a method to predict the local roughness characteristics based on knowledge of the supercooled cloud characteristics, the airfoil geometry, and the icing event time. More specifically, the temporal evolution and the spatial variations of the local roughness maximum height along the airfoil surface are modeled using the product of a scaled time function and spatial function.

$$RMH(t, S_0, LWC, MVD...) = \mathcal{S}(\tau) \mathcal{S}(\sigma) \quad (10)$$

In Eq. (10), $\mathcal{S}(\tau)$ is a function that depends on the icing event time and the supercooled cloud properties related to the impingement process, and $\mathcal{S}(\sigma)$ is function that relates to the surface position, that is its geometry relative to the upstream flow, and to the supercooled cloud properties related to the liquid film dynamics.

The resulting modeling effort is based on the scaling approach of Ruff [24] and follows the development of Tsao and Lee [25] and Tsao and Kreeger [26]. In the scaling-based modeling approach, the formation of roughness in glazed conditions is scaled based on two identified regions of the ice surface each exhibiting different dominant

physical processes. The first region is the stagnation or glaze-ice plateau region that is thought to be dominated by the liquid film dynamics. On the glaze-ice plateau, roughness elements are suspected as being formed by instabilities in the liquid film and grow through liquid migration to low-pressure regions on the film. The second region is formed downstream of the liquid-film breakdown location, which is identified as the edge of the glaze-ice plateau. In the region downstream of the glaze-ice plateau, roughness formation and evolution is thought to be governed by droplet collection physics.

In the Ruff scaling approach, the chord-Reynolds number and the liquid-water density-based Weber number are important. However, because of the importance of the droplet collection physics downstream of the glaze-ice plateau, the first parameter employed in the roughness modeling approach is the Langmuir and Blodgett [27] stagnation point collection efficiency, β_0 , where

$$\beta_0 = \frac{1.4 \left(K_0 - \frac{1}{8} \right)}{1 + 1.4 \left(K_0 - \frac{1}{8} \right)} \quad (11)$$

In Eq. (11), K_0 is the modified inertia parameter of Langmuir and Blodgett [27], defined in Eq. (12),

$$K_0 = \frac{1}{8} + \frac{\lambda}{\lambda_{Sk}} \left(K - \frac{1}{8} \right) \quad (12)$$

which is based on the droplet inertia parameter, K , defined in Eq. (12),

$$K = \frac{\rho_w U_\infty MVD^2}{18 \mu_{air} r_a} \quad (13)$$

and the parameter λ/λ_{Sk} is the droplet range parameter and is further defined as a function of the droplet Reynolds number, $Re_\delta = \rho V MVD / \mu$, as

$$\frac{\lambda}{\lambda_{Sk}} = \frac{1}{0.8388 + 0.001483 Re_\delta + 0.01847 \sqrt{Re_\delta}} \quad (14)$$

Based on the stagnation point collection efficiency, McClain et al. [20] used the local surface collection efficiency estimated using the projected area calculations, as shown in Eq. (15) and based on the schematic of Figure 11, to correlate the roughness variations along the surface.

$$\beta_s = \beta_0 \cos(\gamma_s + AOA) \cos(\Lambda) \quad (15)$$

In Eq. (15), Λ is the wing sweep angle.

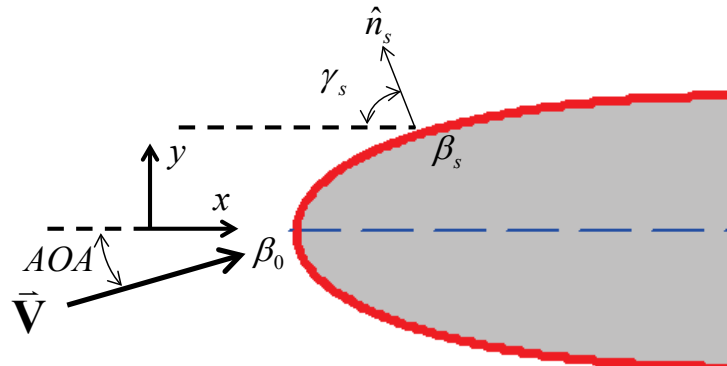


Figure 11. Unswept Airfoil Geometry Relating to the Local Surface Collection Efficiency (β_s) Relative to the Stagnation Point Collection Efficiency (β_0)

To correlate temporal variations in ice roughness and ice thickness, a reference ice thickness must be developed. Using the stagnation point collection efficiency, the volume of water impinging on an incremental area

centered on the leading edge of a wing with sweep angle Λ during an ice accretion event of time Δt_s may be evaluated as

$$dV_{ice} = \frac{LWC \cdot V \cdot \beta_0 \cdot \Delta t_s}{\rho_{ice}} dA \cos(\Lambda) \quad (16)$$

Dividing by the incremental area and multiplying by $2r_0/2r_0$ results in what McClain et al. [20] referred to as the leading edge, fully-dense, theoretical rime ice ($n = 1$) thickness, $N_{\Lambda,R}$.

$$N_{\Lambda,R} = \frac{LWC \cdot V \cdot \beta_0 \cdot \Delta t_s}{\rho_{ice}} \frac{2r_0}{2r_0} \cos(\Lambda) = 2r_0 A_c \beta_0 \cos(\Lambda) \quad (17)$$

where A_c is the unswept-wing accumulation parameter defined in Eq. (1).

The temporal variation component of Eq. (10) has been treated as a linear function based of the leading-edge fully-dense rime-ice thickness, as shown in Eq. (18).

$$\mathcal{J}(\tau) = AMR(\Delta t_s, \text{cloud properties}) = C_t N_{\Lambda,R} \quad (18)$$

In Eq. (18), the airfoil maximum roughness (AMR) is defined as the average of the maximum RMH values on each side of the symmetric airfoils. The coefficient, C_t , in Eq. (18) has been determined to be approximately 0.5 for unswept wings [19]. Further, Figure 12, which is reproduced from McClain et al. [20], presents the airfoil maximum roughness measurements versus the fully-dense rime ice thickness variations for the swept wings investigated by McClain et al. [20]. The dashed line in Figure 12 represents a C_t value of 0.5. Consequently, Eq. (18) has exhibited reasonable agreement with the unswept and swept wing scaling investigations employing a C_t value of 0.5.

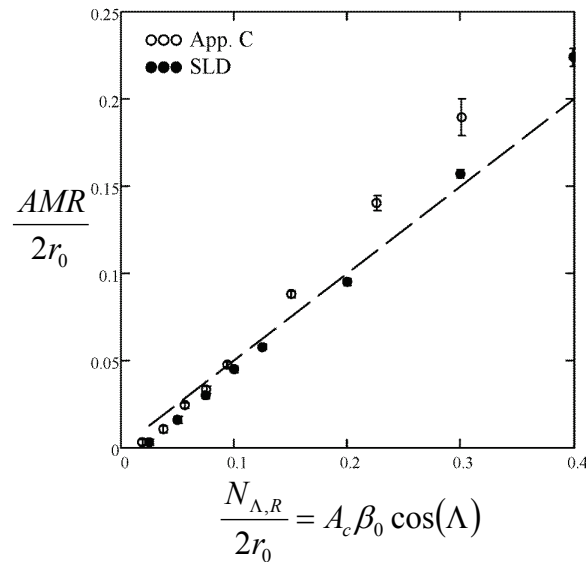


Figure 12. Non-dimensional Temporal Variations in Roughness for Swept Wings [20]

In the collection efficiency dominated roughness region of a glaze ice shape near and aft of the glaze-ice plateau where the surface collection physics are dominant, the spatial variation component of Eq. (10) surface variations are reasonably well described using Eq. (19).

$$\mathcal{S}(\sigma) = \frac{Wei(\beta_s - 0.05, \beta_{fb} - 0.15, 3)}{Wei(0.875(\beta_{fb} - 0.15), \beta_{fb} - 0.15, 3)} + \left(\frac{0.1}{2} - \frac{0.1}{2} \tanh[10(\beta_{fb} - \beta_s)] \right) \quad (19)$$

Where

$$\beta_{fb} = \beta_0 \cos(\gamma_{fb} + AOA) \cos(\Lambda) \quad (20)$$

In Eq. (20), AOA is the angle of attack, and γ_{fb} is surface angle relative to the airfoil design coordinates at the location of the liquid-film break down and ultimately the location of the glaze-ice plateau. Further, $Wei(x, \lambda, k)$ in Eq. (19) is the Weibull probability density function described as

$$Wei(x, \lambda, k) = \frac{k}{\lambda} \left(\frac{x}{\lambda} \right)^{k-1} e^{-(x/\lambda)^k} \quad (21)$$

Where x is a positive real number, λ is referred to as the scale parameter, and k is called the shape parameter or often referred to as the Weibull modulus.

Figure 13 presents the spatial variations of the roughness maximum heights along the surface of scaled unswept wing investigation of McClain et al. [19]. Eq. (19) is represented by the gray, dashed curve in Figure 13. Figure 13 demonstrates reasonable agreement between Eq. (19) and the experimental measurements given the stochastic nature of the ice accretion process. When Eq. (19) was compared to the swept-wing measurements of McClain et al. [20], the measurements were encouraging. While the Weber numbers from the straight-wing study of Ref. [19] were not matched for the swept-wing study of Ref. [20], the roughness surface variations exhibited similar locations of liquid film breakdown, and the form of the roughness surface variations generally agreed with Eq. (19).

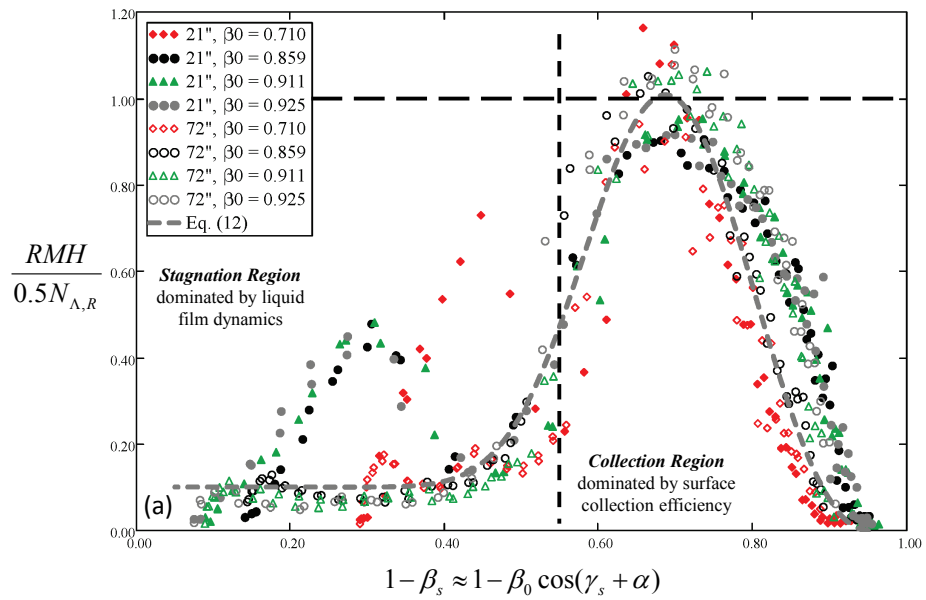


Figure 13. Spatial Roughness Variations on Unswept NACA 0012 Airfoils of Different Sizes [Reprinted from Ref. 19 with permission]

While the initial investigations of ice roughness scaling and modeling have proved encouraging, many issues remain to provide confidence in applying the roughness modeling approach to generalized ice accretion simulation cases. First, the range of freezing fractions employed in this study and in the prior laser-scan ice roughness investigations is 0.19-0.25. Different freezing fractions are expected to affect the roughness surface distribution in three ways: 1) different freezing fractions may lead to different C_t values, 2) different freezing fractions are expected to change the location of the liquid-film breakdown (β_{fb}), and 3) different freezing fractions may increase the width of the roughness distribution which could be accounted for by different values of Weibull modulus. Future efforts are required to determine the importance of and modifications required to account for the effects of different stagnation point freezing fractions on the surface roughness spatial distributions.

Second, all of the roughness modeling and scaling studies reported to this point have been made on unswept and swept wings with symmetric airfoil shapes at 0°-AOA. While symmetric airfoils serve as standard academic test cases, they do not represent wing profile shapes that are expected for future (N+2 and N+3) generations of aircraft such as those envisioned by the NASA Advanced Air Transportation Technology (AATT) Project [28-30]. Modifications are not expected for the temporal scaling associated with lifting airfoils; however, significant modifications to the spatial scaling function of Eq. (19) may be required once significant circulation is imposed on the flow by the airfoil.

Finally, the temporal and spatial scaling functions of Eqns. (18) and (19) focus primarily on the roughness region dominated by collection efficiency physics. On the surface of the glaze ice near the leading edge, the development of roughness is thought to be related to liquid-film instabilities. To predict roughness evolution and spatial variations in the surface of the glaze ice region a new scaling method, potentially following the scaling approach of Anderson and Feo [31], may be required.

5. Conclusions

The acquisition, refinement, and maturation of a three-dimensional, laser-scanning system for ice shapes created in the IRT has been transformative for the study of ice accretion roughness. Coupled with the SOM-based approach of McClain and Kreeger [16] for mean profile identification and roughness quantification, the laser-scanning system has enabled substantial new insights into the characteristics of ice roughness and physics governing ice roughness evolution. The laser scanning system has been used to revisit ice roughness investigations performed in the IRT in the 1990's as well as expand those investigations to the SLD icing regime. The most recent roughness investigations have been based on scaling approaches in an attempt to develop methods to predict the transient variations in roughness characteristics at each point along a wing surface. The most significant findings from the recent 3D laser-scan-based roughness investigations are:

- 1) In early-stage icing, glaze ice accretion roughness increases with increasing accumulation parameter or increasing theoretical rime ice thickness as opposed to reaching a constant roughness height.
- 2) A better understanding of the physics creating the smooth and rough zones identified in the roughness studies of the 1990's has been developed based on the spatial relationship to the glaze ice region near the leading edges of wings and surfaces.
- 3) The glaze-ice scaling investigations have demonstrated that the spatial variations in roughness are related to the location of the glaze-ice plateau, further postulated to be the location of the liquid-film breakdown, and to the droplet collection efficiency variations along the surface.
- 4) Swept-wing scaled roughness evolution and spatial variations have exhibited similarities to unswept-wing roughness evolution and spatial variations, which indicates that while the resulting ice shapes at longer ice accretion event times may be very different, the roughness that forms on a swept wing during an early-stage ice accretion is evolving from the same physical mechanisms that govern roughness evolution on unswept wings.

While the initial roughness and roughness scaling investigations on unswept and swept wings have been promising and enlightening, future experiments are needed to create broader understanding of the physics related ice accretion roughness evolution and spatial variations on aircraft surfaces. To expand the correlation range of validity and to enable broader confidence in future aircraft design, future roughness investigations are recommended focusing on 1) a range of stagnation point freezing fractions, 2) asymmetric airfoils at lifting angles of attack, and 3) scaling approaches developed to reflect the liquid-film physics which is suspected of occurring near the leading-edge of wings in flows with low values of stagnation point freezing-fraction.

Nomenclature

A_c	= accumulation parameter
AOA	= angle of attack
AMR	= airfoil maximum roughness, the maximum of the RMH values along an airfoil or wing surface
b	= codebook vectors
C_t	= coefficient related to the transient scaling function (≈ 0.5)
$h(i,j)$	= neighborhood function of i to j codebook vectors
J	= the number of surface points in the neighborhood of a specific SOM codebook vector
j	= codebook vector index
K	= droplet inertia parameter
L	= length scale related to the Stokes number
LWC	= liquid water content [gm/m^3]
MVD	= median volumetric diameter [μm]
N	= airfoil or mean ice shape surface normal coordinate direction
N_{x^j}	= the orthogonal distance from a surface point (x^j) to the mean surface manifold as described by the SOM codebook vectors
$N_{\Lambda,R}$	= fully-dense Rime ice surface-orthogonal thickness on swept wings
\bar{N}_0	= the measured ice orthogonal-thickness at each codebook vector relative to the clean wing surface
$\bar{N}_{0,AL}$	= the measured attachment line orthogonal-thickness relative to the clean airfoil or wing surface
n	= stagnation point freezing fraction
RMH	= 99%-Gaussian roughness maximum height evaluated at each codebook vector ($=3.09R_q$)

R_q	= the root-mean-square or “standard deviation” roughness height
r_0	= leading edge radius of curvature
SOM	= self-organizing map
S	= mean ice shape surface tangential coordinate direction projected in X-Y plane of wind tunnel
S'	= mean ice shape surface tangential coordinate direction projected in X'-Y' plane of airfoil
S_0	= the clean airfoil tangential coordinate direction and distance projected in X-Y plane of wind tunnel
S_0'	= the clean airfoil tangential coordinate direction and distance projected in X'-Y' plane of airfoil
$\mathcal{S}(\sigma)$	= spatial scaling function
$\mathcal{S}(\tau)$	= Transient (time-based) scaling function
T_{total}	= the freestream stagnation or total temperature
V	= freestream velocity
V_{ice}	= volume of ice
x	= element of point cloud data set
X	= the wind tunnel streamwise coordinate direction
X'	= the airfoil streamwise design coordinate direction
Y	= the wind tunnel streamwise and spanwise orthogonal coordinate direction
Y'	= the airfoil streamwise and spanwise orthogonal design coordinate direction
Z	= the wind tunnel spanwise coordinate direction
Z'	= the airfoil spanwise design coordinate direction
α	= local direction angle of manifold through a codebook vector or airfoil angle of attack
β_{fb}	= local surface collection efficiency at the location of the liquid-film breakdown
β_s	= local surface collection efficiency
β_0	= straight wing stagnation collection efficiency
β_Λ	= swept wing attachment-line collection efficiency
γ	= direction angle of surface point relative to manifold direction through winning codebook vector
γ_s	= direction angle of a surface point relative to the airfoil design coordinates
γ_{fb}	= direction angle of the surface point of liquid-film break down relative to the airfoil design coordinates
Δt_s	= the ice accretion event time
Λ	= wing sweep angle
ρ_{ice}	= density of ice
ρ_w	= density of liquid water
σ	= scaled position parameter
τ	= scaled time parameter
μ_{air}	= viscosity of air

Acknowledgements

The efforts reported in this paper were partially supported as part of NASA Collaborative Agreements No. NNX12AB85A and NNX16AN32A. The support provided through the NASA Advanced Air Transportation Technology (AATT) Project is greatly appreciated. The authors thank Mr. Richard E. Kreeger, Mr. Quentin Schwinn, and Ms. Jordan Salkin for their assistance with the study. Any opinions presented in this paper are those of the authors and do not reflect the views of NASA or the United States government.

References

- [1] Reehorst, A. L., and Richter, G. P., 1987, New Methods for Molding and Casting Ice Formations, NASA Technical Memorandum 100126.
- [2] Hanson, M. K., and Lee, J. D., 1986, Documentation of Ice Shapes Accreted on the Main Rotor of a UH-1H Helicopter in Level Flight, NASA Contractor Report 175088.
- [3] Lee, J.D., Berger, J.H., and McDonald, T.J., 1986, Wind Tunnel Tests of Rotor Blade Sections with Replications of Ice Formations Accreted in Hover, NASA Contractor Report 175089.
- [4] Kind, R.J., Potapczuk, M.G., Feo, A., Golia, C., and Shah, A.D., 1998, *Experimental and Computational Simulation of In-Flight Icing Phenomena*, Elsevier Science Ltd., 0376-0421/98.
- [5] Vannuyen, T., 1998, *Process Developed for Forming Urethane Ice Models*, Technical Report, NASA Lewis Research Center, 20050181946.
- [6] Han, Y. and Palacios, J., 2014, Transient Heat Transfer Measurements of Surface Roughness due to Ice Accretion, 6th AIAA Atmospheric and Space Environments Conference, 16-20 June, Atlanta, GA, AIAA-2014-2464.

[7] Shin, J., 1994, Characteristics of Surface Roughness Associated With Leading Edge Ice Accretion, NASA TM-106459.

[8] Anderson, D. N., and Shin, J., 1997, Characterization of Ice Roughness from Simulated Icing Encounters, NASA TM-107400.

[9] Anderson, D. N., Hentschel, D. B., and Ruff, G. A., 1998, Measurement and Correlation of Ice Accretion Roughness, NASA CR—2003-211823.

[10] Broeren, A.P., Addy, H.E. Jr., Lee, S., and Monastero, M.C., 2014, Validation of 3-D Ice Accretion Methodology for Experimental Aerodynamic Simulation, NASA/TM-2015-218724, AIAA-2014-2614.

[11] Wright, W., 2008, User's Manual for LEWICE Version 3.2, NASA/CR—2008-214255.

[12] Lee, S., Broeren, A., Addy, H., Sills, R., and Pifer, E., 2012, Development of 3D Ice Accretion Measurement Method, AIAA-2012-2938, presented at the 4th AIAA Atmospheric and Space Environments Conference, June 25-28.

[13] Lee, S., Broeren, A. P., Kreeger, R. E., Potapczuk, M., and Utt, L., 2014, Implementation and Validation of 3-D Ice Accretion Measurement Methodology, 6th AIAA Atmospheric and Space Environments Conference, June 16-20, Atlanta, GA, AIAA-2014-2613.

[14] Broeren, A.P., Addy, H.E., Lee, S., and Monastero, M.C., 2014, Validation of 3-D Ice Accretion Measurement Methodology for Experimental Aerodynamic Simulation, 6th AIAA Atmospheric and Space Environments Conference, June 16-20, Atlanta, GA, AIAA-2014-2614.

[15] Kreeger, R.E. and Tsao, J.-C., 2014, Ice Shapes on a Tail Rotor, 6th AIAA Atmospheric and Space Environments Conference, June 16-20, Atlanta, GA, AIAA-2014-2612.

[16] McClain, S.T., and Kreeger, R.E., 2013, Assessment of Ice Shape Roughness Using a Self-Organizing Map Approach, Presented at the 5th AIAA Atmospheric and Space Environments Conference, June 24-27, San Diego, CA, AIAA-2013-2546.

[17] McClain, S.T., Reed, D., Vargas, M., Kreeger, R.E., and Tsao, J.-C., 2014, Ice roughness in Short Duration SLD Icing Events, Presented at the 6th AIAA Atmospheric and Space Environments Conference, June 16-20, Atlanta, GA, AIAA-2014-2330.

[18] McClain, S.T., Vargas, M., Kreeger, R.E., and Tsao, J.-C., 2015, A Reevaluation of Appendix C Ice Roughness Using Laser Scanning, SAE 2015 International Conference on Icing of Aircraft, Engines, and Structures, June 22-25, Prague, Czech Republic, SAE2015-01-2098.

[19] McClain, S.T., Vargas, M., and Tsao, J.-C., 2016, Characterization of Ice Roughness Variations in Scaled Glaze Icing Conditions, 8th AIAA Atmospheric and Space Environments Conference, June 13-17, Washington, DC, AIAA-2016-3592.

[20] McClain, S.T., Vargas, M., and Tsao, J.-C., 2017, Ice Roughness and Thickness Evolution on a Swept NACA 0012 Airfoil, 9th AIAA Atmospheric and Space Environments Conference, June 5-9, Denver, CO, AIAA-2017-3585.

[21] Kohonen, T., 2001, *Self-Organizing Maps*, Berlin: Springer-Verlag, 3rd ed.

[22] McClain, S., Tino, T., and Kreeger, R., 2011, Ice Shape Characterization Using Self-Organizing Maps, *Journal of Aircraft*, Vol. 48, No. 2, March-April.

[23] McClain, S.T., 2016, Manual Point Cloud Registration for Combined Ice Roughness and Ice Thickness Measurements, 8th AIAA Atmospheric and Space Environments Conference, June 13-17, Washington, DC, AIAA-2016-3590.

[24] Ruff, G.A., 1986, Analysis and Verification of the Icing Scaling Equations, AEDC-TR-85-30, vol. 1 (Rev), March 1986.

[25] Tsao, J.C. and Lee, S., 2012, Evaluation of Icing Scaling on Swept NACA 0012 Airfoil Models, NASA/CR—2012-217419, May 2012.

[26] Tsao, J.C. and Kreeger, R.E., 2009, Experimental Evaluation of Stagnation Point Collection Efficiency of the NACA 0012 Swept Wing Tip, AIAA-2009-4125 and NASA/TM-2010-216102, March 2010.

[27] Langmuir, I. and Blodgett, K. B. 1946, A Mathematical Investigation of Water Droplet Trajectories, Army Air Forces Technical Report No. 5418.

[28] Bruner, S. et al., 2010, NASA N+3 Subsonic Fixed Wing Silent Efficient Low-Emissions Commercial Transport (SELECT) Vehicle Study: Revision A, NASA Technical Report NASA/CR-2010-216798.

[29] Gur, O., Bhatia, M., Schetz, J. A., Mason, W. H., Kapania, R. K., and Mavris, D. N., 2010, Design Optimization of a Truss-Braced-Wing Transonic Transport Aircraft, *Journal of Aircraft*, Vol. 47, No. 6, pp. 1907–1917.

[30] Drela, M., 2011, Development of the D8 Transport Configuration, 29th AIAA Applied Aerodynamics Conference, 27-30 June, Honolulu, HI, AIAA-2011-3970.

[31] Anderson, D. and Feo, A., 2002, Ice-accretion scaling using water-film thickness parameters, 40th AIAA Aerospace Sciences Meeting & Exhibit, Aerospace Sciences Meetings, Reno, NV, AIAA-2002-0522.